PAPER
Anton Ginzburg, Dilhan Kandemir, Peter Van Puyvelde *et al*.
Synthesis of thermo-shear-responsive dynamic covalent
networks based on humins and the Diels–Alder reaction

Check for updates

Synthesis of thermo-shear-responsive dynamic covalent networks based on humins and the Diels–Alder reaction

Dilhan Kandemir,[a] Meghana Mekala, [ID][b] Ruth Cardinaels, [ID][b] Peter Van Puyvelde[b] and Anton Ginzburg [ID] ⋆[a]

Humins are abundant yet largely underutilised by-products of sugar-based biorefineries, commonly regarded as low-value waste streams despite their intrinsically furan-rich structure. By leveraging their furan-rich architecture, we demonstrate that humins can serve as a versatile and sustainable source of dienes in Diels–Alder (DA) chemistry when employed directly as reagents. We show that they readily form dynamic covalent networks upon reaction with conventional dienophiles, such as bismaleimides, under mild conditions. Notably, the cycloaddition proceeds predominantly *via* an *endo*-selective pathway. Moreover, the DA equilibrium exhibits an unconventional, inverted thermo-mechanical response under oscillatory shear, with the forward reaction favored at elevated temperatures and the retro-DA reaction promoted at lower temperatures. The resulting materials exhibit tunable thermal and mechanical properties, self-healing behaviour, and chemically controllable electrical conductivity. Taken together, our findings establish a practical pathway for converting biorefinery side streams into value-added functional materials.

Green foundation

1. Our study advances green chemistry by combining renewable feedstock utilisation with new fundamental insights into a classical Diels–Alder (DA) reaction. We demonstrate the efficacy of using a bio-derived reagent, humins, in substantial amounts directly as a diene source in the DA reaction under mild conditions. This reagent not only participates in the cycloaddition, offering a green alternative, but also imparts unique and noteworthy features: the cycloaddition is highly stereoselective (*endo*) and it exhibits an unconventional DA/retroDA equilibrium, making this study compelling from both a sustainability perspective and a fundamental chemistry standpoint.

2. We report successful reactions using up to 75 wt% humins, advancing green chemistry through renewable feedstock utilisation.

3. While the dienophile remains conventional, future work should extend this strategy to biobased dienophiles to achieve fully renewable DA-systems. Further optimisation should also target solvent minimisation.

Introduction

The Diels–Alder (DA) reaction is a well-established and extensively studied transformation in organic chemistry, involving a [4 + 2] cycloaddition between conjugated dienes and dienophiles to form six-membered ring structures.[1–3] Due to its complete atom economy and high regio- and stereoselectivity, the DA reaction is regarded as an efficient "click" strategy for the construction of functional and dynamic molecular and macromolecular systems.[4,5] Reflecting its versatility, a wide range of π-systems can serve as dienophiles in DA reactions, including alkenes,[6] alkynes,[7] azomethines,[8] nitriles,[9] carbonyl compounds,[10] thiocarbonyls,[11] azo compounds,[12] singlet oxygen,[13] and nitro compounds.[14] Even greater diversity is observed amongst dienes, which can incorporate various electron-donating or electron-withdrawing substituents, allowing for a systematic modulation of reactivity and selectivity in the cycloaddition process.[15–17]

Despite its significant potential, the number of commercially impactful applications of the DA reaction in speciality polymers remains limited.[18] This limitation is partly attributable to the high cost of the building blocks typically used in DA chemistry to manipulate final rheological characteristics, such as chain extenders (*e.g.*, poly(propylene glycol) bis(2-aminopropyl ether)[19]). Concurrently, the growing emphasis on sustainability in the chemical industry underscores the urgent

*[a]Department of Chemical Engineering, Soft Matter, Rheology, and Technology, KU Leuven, Wetenschapspark 27, 3590 Diepenbeek, Belgium.
E-mail: anton.ginzburg@kuleuven.be*
[b]Department of Chemical Engineering, Soft Matter, Rheology, and Technology, KU Leuven, Celestijnenlaan 200J, 3001 Heverlee, Belgium

need to identify and develop alternative, renewable feedstocks. In this context, bio-based, furan-rich compounds derived from biorefinery streams have emerged as especially promising candidates. Yet, research in this area remains limited and lacks representative, well-characterised systems.[20–23]

The acid-catalysed dehydration of D-fructose is an industrially relevant process for producing bio-renewable compounds, including furfural, 5-hydroxymethylfurfural (HMF), levulinic acid (LA), and formic acid. However, the overall efficiency and scalability of this method are significantly affected by the production costs and by how these bio-based approaches compare economically to traditional petrochemical routes.[24,25] A major challenge lies in the formation of substantial by-products, humins, that emerge in side reactions such as aldol condensation and transesterification. These humins can account for up to 50% of the total carbon during the biorefinery process, thereby impacting the process yield and viability. While various structural models have been proposed in the literature,[26,27] all reports consistently describe humins as poly-furan-based frameworks substituted with diverse motifs bearing hydroxyl, aldehyde, and ketone functional groups.[28–30]

In this work, we explore a new application area of humins based on a simple concept: their diverse furan-ring structures provide an alternative and versatile source of dienes for DA chemistry. We show that pairing humins with maleimides can form covalent macromolecular networks that are reprocessable and can be repaired under mild and oscillatory shear conditions, where the applied deformation cooperates with temperature to promote reversible bond exchange. This behaviour represents a thermomechanical analogue of DA reactivity observed in molecular systems.[31] Notably, we observe a highly *endo*-selective cycloaddition. The temperature-dependent equilibrium between DA and retro-DA further enables repetitive processing and structure recovery with minimal loss of properties. We show that this approach can be applied to multiple, unmodified, industrial humins batches and tolerates high humins loadings. In addition, we demonstrate that the DA crosslinking provides a direct handle on the electrical properties, reducing conductivity and enabling thermally switchable dielectric behaviour.

Results and discussion

Characterisation of different humins and model reaction (furfuryl alcohol-bismaleimide system)

This study evaluates the applicability and performance of four distinct batches of industrial humins (Humins1 through Humins4), generated as side-stream products in the acid-catalysed dehydration of D-fructose. All batches originate from the same industrial process but represent independent production runs. Despite exhibiting a comparable furan-rich backbone architecture, as evidenced by consistent spectroscopic signatures in solution ^{1}H NMR (Fig. 1A), the humins exhibit substantial differences in zero-shear viscosity (Fig. 1B and

Fig. S23–S29: η_0(Humins1) = 4020 Pa s; η_0(Humins2) = 958 Pa s; η_0(Humins3) = 896 Pa s; η_0(Humins4) < 10 Pa s).

The ^{1}H NMR spectra of the humins batches (Fig. 1A and Table S1) display broad, strongly overlapping resonances typical of heterogeneous, crosslinked furan-based materials. Because individual proton environments cannot be quantitatively resolved, our analysis is restricted to assigning chemical-shift regions rather than discrete molecular species. For semi-quantitative comparisons, the spectra were recorded in DMSO-d_6 at comparable sample concentrations (Table S2), enabling a comparison of the aromatic/furanic region across the humins batches. A weak signal at 9.2–9.0 ppm is consistent with alde-hydic or strongly hydrogen-bonded OH protons. The broad resonances between 7.5 and 6.8 ppm can be attributed to aromatic and furanic protons, confirming the presence of substituted furan motifs. The signals in the 4.8–3.2 ppm region are assigned to protons on oxygen-substituted carbons (–CH–O–, –CH$_2$–O–), characteristic of structural motifs derived from FA, HMF, and furfural, in agreement with the literature,[30] which describes humins as polyfuranic networks. The broad envelope between 2.8 and 1.3 ppm reflects contributions from aliphatic segments adjacent to carbonyl or oxygenated sites, as well as methylene environments incorporated within aliphatic linkers. Taken together, the spectra are consistent with previously established structural models of humins. Although the main spectral features are conserved across all batches, Humins4 shows relatively stronger signals in the aliphatic and oxygenated-carbon regions, which may explain its lower viscosity and differences in molecular organisation. Such compositional variations are certainly to be expected during sugar processing, where the exact composition depends on the processing conditions, dehydration severity and residence time. FTIR analysis confirmed the preservation of the average chemical motif across batches (Fig. S1) with characteristic absorptions including a broad OH-stretching of alcohols at around 3383 cm^{-1}, aliphatic CH-stretching at about 2934 cm^{-1}, and C=O stretching vibrations of aldehyde groups attached to hydroxymethylfurfural (HMF) and 5-methoxymethylfurfural (MMF) at about 1670 cm^{-1}. Interestingly, the spectrum also displays the product of the aldol condensation reaction, a conjugated enone, which can be detected via the C=C stretching conjugated with the carbonyl group at 1615 cm^{-1}. Additional contributions to the spectrum can be attributed to substituted furan rings, such as C=C stretching at 1517 cm^{-1} and C–H bending at 1077 cm^{-1}. The C–O stretching observed at 1020 cm^{-1} can also be attributed to the furan ring. The substituted furans may also be related to CH out-of-plane deformations between 812 and 749 cm^{-1}. Finally, the 966 and 904 cm^{-1} peaks are commonly associated with *trans*- and *cis*-C=C configurations, respectively. These structural assignments are well in line with the literature references.[28,32]

Although relative differences are observed, all humins batches exhibit comparable estimated furanic signal contributions, within the same order of magnitude. This spectral profile is particularly important from the perspective of our
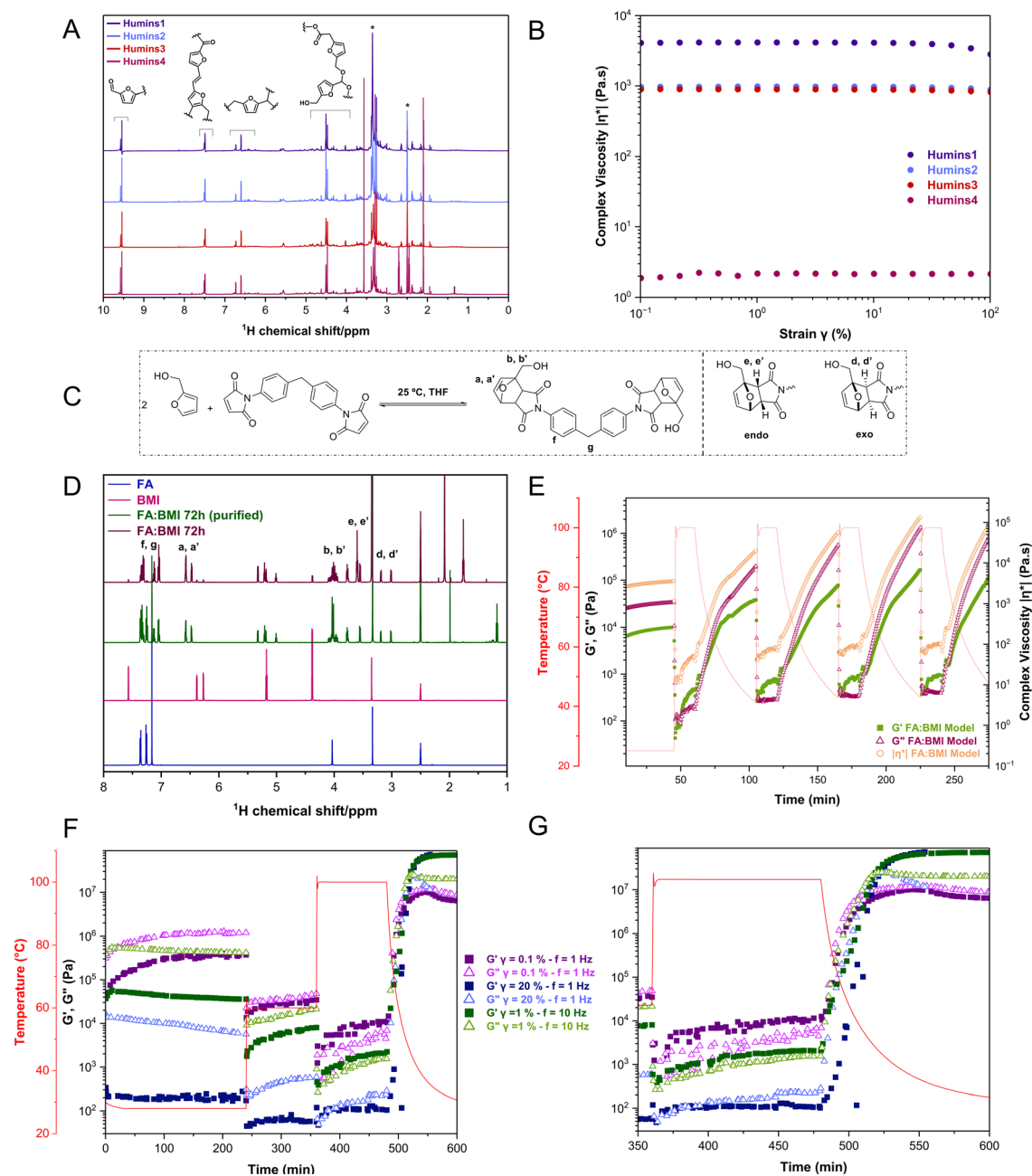
Fig. 1 (A) ^{1}H NMR spectra of representative humins batches (Humins1–4) recorded in DMSO-d6 at 25 °C, (B) amplitude sweep analysis of humins batches at strain of 0.01–100%, constant frequency of 1.6 Hz and experimental temperature of 25 °C, (C) Diels−Alder reaction scheme of furfuryl alcohol (FA) and bismaleimide (BMI), forming the corresponding *endo/exo* adducts; (D) ^{1}H NMR spectra of FA, BMI, and their DA adducts after 72h (unpurified and purified) in DMSO-d6 at 25 °C, (E) temperature-modulated small-amplitude oscillatory shear (SAOS) measurements of FA : BMI model system using a 25 mm parallel-plate geometry (γ = 0.1%, f = 1 Hz, 2 °C min^{-1}, N$_2$ atmosphere), (F and G) dynamic temperature-ramp tests of the FA : BMI model system at different combinations of strain and frequency (i) γ = 0.1% − f = 1 Hz, (ii) γ = 20% − f = 1 Hz and (iii) γ = 1% − f = 10 Hz using a 25 mm parallel-plate geometry (2 °C min^{-1}, N$_2$ atmosphere).

DA-oriented study. Overall, the data suggest that humins consist of a distribution of substituted furan ring structures with varying steric accessibility, ranging from terminal furan units to more heavily substituted furanic motifs, predominantly at positions 2 and 5 and to a lesser extent at positions 3 and 4.

In an effort to evaluate the relative percentage of furan-associated groups in humins, we employed a calibration-based approach using the characteristic C−O−C stretching mode of the furan moiety at 1025 cm^{-1}. In selecting a model compound, we reasoned that HMF provides a logical starting point, given its established role as a key intermediate in

humins formation and its contribution to the furanic motifs embedded within the resulting polymeric network. At the same time, in our previous study, we identified hydroxyl functionalities – most plausibly associated with FA-type fragments – as the reactive sites in acylation reactions.[29] Accordingly, FA was chosen as the internal standard. THF solutions were prepared at different concentrations and characterized by ATR-FTIR. Interestingly, high viscosity Humins1 exhibited a slope closely matching that of the FA calibration solutions, corresponding to an apparent FA-equivalent signal of approximately 60 wt% (Fig. S2–S4). In contrast, the remaining lower viscosity humins batches displayed distinctly different calibration responses, suggesting structural differences. On the other hand, C–O–C stretch in a furan ring typically appears around 1010–1050 cm^{-1}, but its exact position and intensity are sensitive to electronic effects (electron-donating/withdrawing groups) and steric hindrance. Added to this, the absorbance might be further influenced by non-furanic components like ether linkages. Therefore, this calibration cannot be used to determine the absolute furan content of humins, but rather serves as a semi-quantitative FA-equivalent spectroscopic reference. As a control experiment, we evaluated the integrals of furanic signals in ^{1}H NMR at $\delta(^1\mathrm{H})$ = 7.6–6.2 ppm (Table S3) and The total furan content appeared to increase in the following order: Humins1 < Humins3 < Humins2 < Humins4, which reasonably agrees with the FTIR-based comparison when considering a similar concentration range as in the NMR experiments (30–32 mg mL^{-1}).

Regarding the choice of dienophiles, it is well established that electron-deficient dienophiles such as maleimides exhibit high reactivity in DA cycloadditions with numerous bio-based furans. Notably, some of these reactions proceed efficiently under solvent-free and catalyst-free conditions. Moreover, the furan (diene)–maleimide (dienophile) pair is frequently selected for DA reactions due to its ability to proceed at ambient temperature.[33–36] Following this rationale, 1,1′-(Methylenedi-4,1-phenylene)bismaleimide (BMI) was selected as the corresponding dienophile. Initially, model reactions were carried out using varying equivalents of the reactants (Fig. S5 and S6) and different reaction times at room temperature (Fig. S7 and S8). The progress of the reactions was monitored by tracking the characteristic peaks of BMI and FA.[1,4,32]

For the BMI, these included the overtone/combination band around 1904 cm^{-1} characteristic of the maleimide moiety, the C=O stretch between 1700–1774 cm^{-1}, the C=C stretch at 1602 cm^{-1}, and peaks between 686–826 cm^{-1} attributed to aromatic C–H out-of-plane bending vibrations. FA displayed peaks at 3400–3200 cm^{-1} for O–H stretching, 1600–1450 cm^{-1} for C=C stretching in the furan ring, and 1200–1100 cm^{-1} for C–O stretching. Following the DA reaction, significant spectral changes were observed. The disappearance of the 1904 cm^{-1} peak in BMI indicated alterations in the electronic environment of the maleimide carbonyl groups, while the C=O stretch shifted or intensified, reflecting formation of the DA adduct. The reduction in intensity of the 1602 cm^{-1} peak suggested participation of these double bonds n σ-bond

formation during the DA reaction. New bands appeared at 1380 cm^{-1} (C–N stretching) and 1180 cm^{-1} (C–C/C–O related vibrations), consistent with the formation of the Diels–Alder adduct. Additionally, the peaks between 686–826 cm^{-1}, corresponding to the BMI, were diminished.

The ^{1}H NMR spectrum of the product from the reaction between furan and bismaleimide at a 2:1 molar ratio showed characteristic peaks consistent with the expected DA-adduct structure (Fig. 1C and D). Specifically, the presence of aliphatic signals at $\delta(^1\mathrm{H})$ = 3.1–3.5 ppm and $\delta(^1\mathrm{H})$ = 3.7–3.8 ppm is consistent with the formation of new proton environments arising from the DA cycloaddition. At the same time, the residual BMI persisted even after a 72 h reaction time, as evidenced by the presence of aromatic protons at $\delta(^1\mathrm{H})$ ~7.3–7.4 ppm, indicating incomplete conversion. While most of the tests were conducted without removing residual BMI, a control experiment was performed in which the product was purified by column chromatography, and the conversion was estimated. After normalisation to the constant aromatic protons of BMI (δ 7.35–1.04 ppm, 8H), the DA product signals in the aliphatic region integrated to 1.45 H for the *endo* resonances (δ 3.77 and 3.56 ppm) and 0.67 H for the *exo* resonances (δ 3.18 and 3.01 ppm), giving a total product integral of 2.12 H. Since the expected contribution of the DA product signals in this system is 4H, the apparent solution-state conversion referenced to the BMI aromatic protons resulted in $X_{\mathrm{DA,product}}$ = 2.12/4 = 53%, which is in good agreement with literature reports for furan–maleimide systems under comparable mild conditions.[37,38] It is well established that under kinetic control, the *endo* DA adduct is often favoured due to stabilising secondary orbital interactions between the π-system of the diene and electron-withdrawing substituents on the dienophile, which can stabilise the *endo* transition state relative to that of the *exo* state. In contrast, thermodynamic control often enriches the *exo* isomer as steric and substituent effects dominate the equilibrium. Substituents on the furan ring, such as carbonyl and hydroxyl groups, modulate both rate and diastereoselectivity. For example, DFT studies have suggested that hydroxyl groups can thermodynamically stabilise the *endo* isomer by promoting intramolecular hydrogen bonding and dispersive interactions within the transition state, thereby reducing the activation free energy and facilitating cycloaddition.[39,40] In line with these literature trends, the ^{1}H NMR spectrum of the purified FA:BMI model product revealed an *endo*:*exo* ratio of 68:32, in good agreement with previously published results.[41] It should be noted, however, that all NMR measurements were performed in DMSO-d6 solution; therefore, the observed *endo* and *exo* resonances reflect the apparent distribution in solution rather than the exact equilibrium composition in the bulk material. Moreover, as the reaction mixture was not purified, these signals represent the apparent distribution within the crude equilibrium mixture rather than that of isolated stereoisomers.

Under small-amplitude oscillatory shear (SAOS), the unpurified resulting materials derived from the FA:BMI model reaction exhibited a viscoelastic response (Fig. S9 and S10). At low strains (below 2%), the FA:BMI model product demonstrated

a linear viscoelastic response characterised by dominantly viscous properties, with the loss modulus (G'') exceeding the storage modulus (G') (Fig. S11). Structurally, cycloaddition adducts represent dynamic covalent linkages that can be modulated by external stimuli such as temperature and mechanical deformation. However, to the best of our knowledge, and despite the long-standing and extensively studied DA chemistry, the application of rheological methods remains underexplored, especially for small-molecule DA model systems.[42,43] Some studies have indeed investigated reversible DA systems under rheological or mechanical conditions in polymer or network contexts,[19,44,45] but these focused primarily on prepolymers or crosslinked materials rather than small-molecule adducts.

Motivated by this gap, we further explored this dynamic behaviour by performing temperature-dependent rheology under mild oscillatory conditions ($\gamma = 0.1\%$, $f = 1$ Hz) between 30–60–100–30 °C (Fig. 1F and Table S3). Upon heating between 30 and 60 °C, the moduli and complex viscosity decreased gradually, while the material remained a viscoelastic fluid. Notably, around 100 °C, the storage modulus surpassed the loss modulus ($G' > G''$) with the well-resolved crossover, indicating a transient behaviour toward elastic networks. Upon subsequent cooling, both G'', G', and $|\eta^*|$ recovered to values higher than initial levels, remaining solid-like, evidencing cumulative structural reinforcement. This behaviour was consistently observed in multiple heating–cooling cycles (40–100–40 °C and 60–100–60 °C), where each cycle produced a G'/G'' crossover at 100 °C followed by a progressively higher modulus and viscosity plateaus upon cooling (Fig. 1E and Fig. S12).

Conventionally, it is assumed that the retro DA (rDA) reaction usually occurs at high temperature, whereas the DA reaction proceeds at low temperature. In a previous work,[46] the polymers containing both maleimide and furan moieties as repeating units in a copolymer, in fact, exhibited such reversible behaviour. In contrast, our FA : BMI system showed an opposite response: additional cycloadditions occurred at higher temperatures under oscillatory conditions, while cooling shifted the equilibrium toward rDA. This inversion of the classical DA/rDA behaviour suggests a cooperative interplay between mechanical stress and temperature, in which the DA/rDA equilibrium is not solely temperature-dependent but also sensitive to oscillatory stress. Consequently, stress-assisted DA reformation becomes possible under conditions where rDA would typically dominate. Such FA : BMI system thus operates under coupled thermo-mechanical control, in which mechanical energy facilitates the reversible reformation of bonds and network reinforcement. This behaviour qualitatively resembles recent observations in small-molecule systems where periodic mechanical input can influence thermally reversible DA equilibria; however, the exact mechanism in our system remains to be fully understood.[31,47]

One can further speculate that the oscillatory shear parameters influence the DA/rDA equilibrium. To probe this effect, four distinct combinations of strain amplitude and angular frequency were examined: (i) $\gamma = 0.1\%$ − $f = 1$ Hz, (ii) $\gamma = 20\%$ − $f = 1$ Hz and (iii) $\gamma = 1\%$ − $f = 10$ Hz (Fig. 1F and G) and (iv) $\gamma = 0.1\%$ − $f = 50$ Hz (Fig. S13). At low temperature (30 °C), all conditions resulted in a viscoelastic fluid response. Higher frequencies led to increased storage and loss moduli at low strain amplitudes, whereas larger strain amplitudes reduced both moduli, indicating progressive network deformation. After heating to 60 °C, a gradual increase in the dynamic moduli was observed for all conditions. At 100 °C, the emergence of solid-like behaviour provided a strong indication for thermally and mechanically promoted network formation. Upon subsequent cooling to 30 °C, pronounced differences in the final mechanical state became apparent. Conditions involving either high frequencies ($\gamma = 0.1\%$ − $f = 50$ Hz and $\gamma = 1\%$ − $f = 10$ Hz) or large strains at moderate frequency ($\gamma = 20\%$ − $f = 1$ Hz) yielded materials that behaved as viscoelastic solids at the end of the cycle. In contrast, the low-frequency, low-strain condition (0.1% − $f = 1$ Hz) retained a fluid-like response (Table S3). Taken together, these results demonstrate that both strain amplitude and oscillation frequency act as effective mechanical control parameters, superimposed on temperature, in governing the extent of DA bond formation and the resulting viscoelastic state.

^{1}H NMR analysis further revealed that the FA : BMI adducts continue to evolve over time (Fig. S14 and Tables S4, S5). Between 72 h and four weeks, all DA-related resonances intensified, accompanied by a moderate increase in the fraction of *exo* adducts, suggesting a slow *endo*/*exo* rearrangement and higher overall conversion upon storage. The reference sample used for rheological comparison (four weeks, no shear) exhibited an apparent *endo*/*exo* ratio of ≈36/64 (*endo* = 1.83; *exo* = 3.22). After rheological treatment, both *endo* ($\delta(^1H)$ = 3.60–3.55 ppm, 3.02 ppm) and *exo* ($\delta(^1H)$ = 3.76 ppm, 3.18 ppm) resonances increased in intensity, while the overall ratio remained essentially unchanged (~35/65). For example, after 0.1% γ, 1 Hz, *endo* = 1.87 and *exo* = 3.54; after 20% γ, 1 Hz, *endo* = 1.90 and *exo* = 3.51. These results indicate that oscillatory shear and temperature cycles are associated with increased intensity DA-related resonances due to additional bond formation or redistribution within a reversible network. Within the resolution of the solution-state NMR analysis, no substantial shift in the apparent *endo*/*exo* ratio was detected after rheological treatment, suggesting that the applied thermo-rheological conditions do not significantly alter the apparent stereochemical distribution in solution.

The measured sensitivity of the DA equilibrium to combined thermal and mechanical input in the FA : BMI model system illustrated that even minor perturbations can influence furan-bismaleimide reactivity. Motivated by this responsiveness under oscillatory shear, we subsequently focused our efforts on elucidating the reaction between humins and BMI.

Reaction between humins and bismaleimide

We speculate that the potential DA reactivity of humins is governed primarily by substitution patterns that modulate electron density and steric accessibility at the dienic positions. In

general, steric hindrance in *cis*-configured dienes reduces their effective participation, while favourable substitution at other positions or ring constraints can stabilise reactive conformations. Cyclic *cis*-dienes, in particular, often display enhanced reactivity due to enforced geometries that align the reacting double bonds.[48] Based on the considerations outlined above, it is reasonable to assume that the structural composition and conformational flexibility of the humins backbone are sufficient to enable the DA reaction to occur. Importantly, all experiments were performed using industrial humins as received, without purification or fractionation. The optimisation of reaction conditions using model systems involved determining the humins : BMI ratio by varying feed ratios and controlling the BMI conversion. While calibration with FA provided an estimate of the furan content, detailed optimisation was essential due to the more structurally complex diene source.

Using Humins 1 as a high-molecular-weight precursor, reactions between BMI and 25, 35, and 50 wt% Humins 1 at room temperature yielded solid materials (denoted as DDA1–DDA3; Fig. S15–S17). FTIR analysis confirmed that DA adduct formation occurred in all cases; however, prominent signals of residual BMI remained. We speculate that, under these conditions, network development remains limited, leading to the formation of powdery and crumbly materials (Fig. S19). When 75 wt% Humins1 were used, FTIR analysis revealed a more pronounced DA-related transformation, including a decrease in the BMI-related band at 1602 cm^{-1} (Fig. 2 and Fig. S18) and the appearance of new carbonyl bands between 1700–1774 cm^{-1}, indicating the formation of new C=O bonds. Additionally, characteristic signals of the DA reaction were observed at 1180 cm^{-1} and 1150 cm^{-1}, corresponding to C–O–C and C–C stretching modes, respectively, along with a peak at 1380 cm^{-1} attributed to C–N stretching from the newly formed DA adducts. The resulting end product was a putty-like material. Similar to the model reaction, 72 hours proved to be the most suitable reaction time, as the characteristic peaks associated with the DA reaction were most pronounced in the sample reacted for 72 hours (Fig. S20). Moreover, the viscosity and bleeding issues initially observed after the 24- and 48-hour reactions were no longer present after 72 hours.

The ^{1}H NMR spectra of the Humins1 and DDA4-75% Humins1 (putty-like) samples (Fig. 3B) reveal key chemical changes resulting from the DA reaction with BMI. Notably, the reaction primarily exhibits resonances assignable to *endo*-type adducts, while signals associated with *exo* analogues were not detected within the resolution of our spectra. This assignment is supported by resonances observed in the range $\delta(^{1}\text{H})$ = 3.7–4.0 ppm and by the absence of signals at $\delta(^{1}\text{H})$ = 3.1–3.5 ppm. While definitive stereochemical assignment in such structurally heterogeneous systems remains challenging, the apparent predominance of *endo*-type signals may reflect the influence of steric constraints and conformational restrictions imposed by the polyfuranic humins backbone during the cycloaddition, warranting further investigation using broader structural platforms. In the $\delta(^{1}\text{H})$ = 4.8–3.2 ppm range,
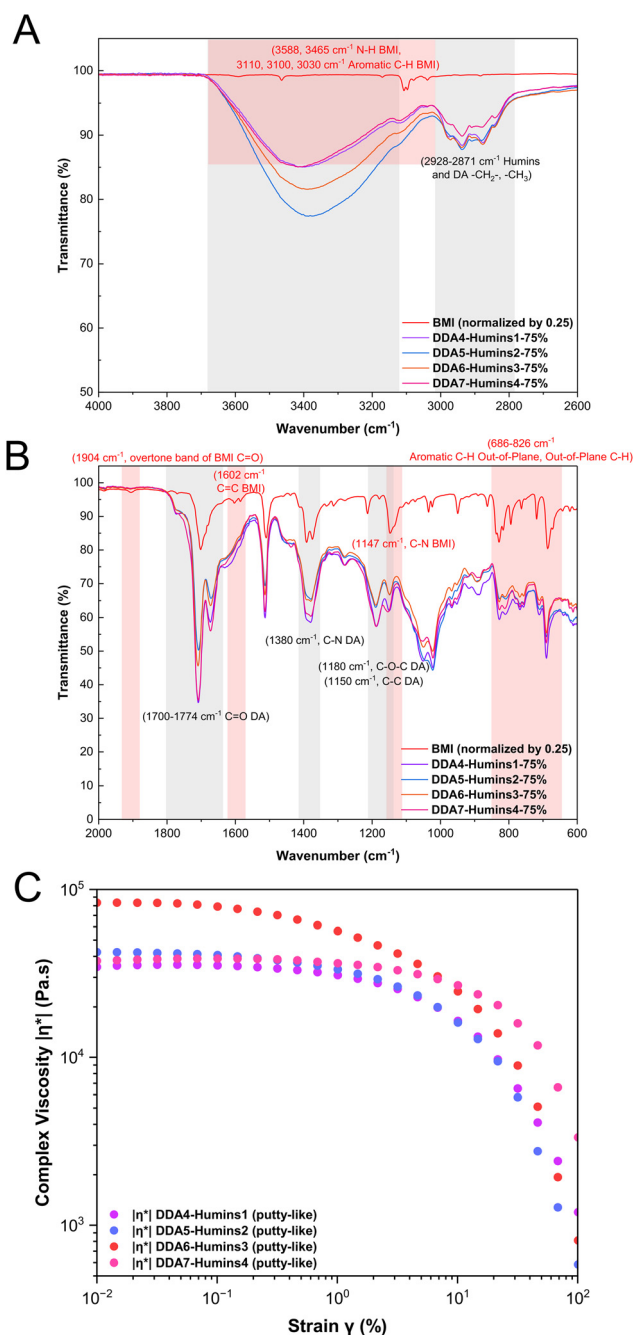
Fig. 2 (A) ATR-IR spectra of BMI and Diels−Alder adducts derived from four different humins feedstocks (DDA4-Humins1-75%, DDA5-Humins2-75%, DDA6-Humins3-75%, DDA7-Humins4-75%) recorded at room temperature, shown for the 4000−2600 cm^{-1} region (B) and the 2000−600 cm^{-1} region (C); (C) amplitude sweep analysis of the humins batches over a strain range of 0.01–100%, at a constant frequency of 1.6 Hz and experimental temperature of 25 °C.

additional resonances correspond to protons attached to oxygenated carbons, such as hydroxyl, ether, or ester groups, characteristic of residual carbohydrate-derived structures and oxygenated species formed during the reaction. The signals between $\delta(^{1}\text{H})$ = 2.8–2.4 ppm are attributed to aliphatic
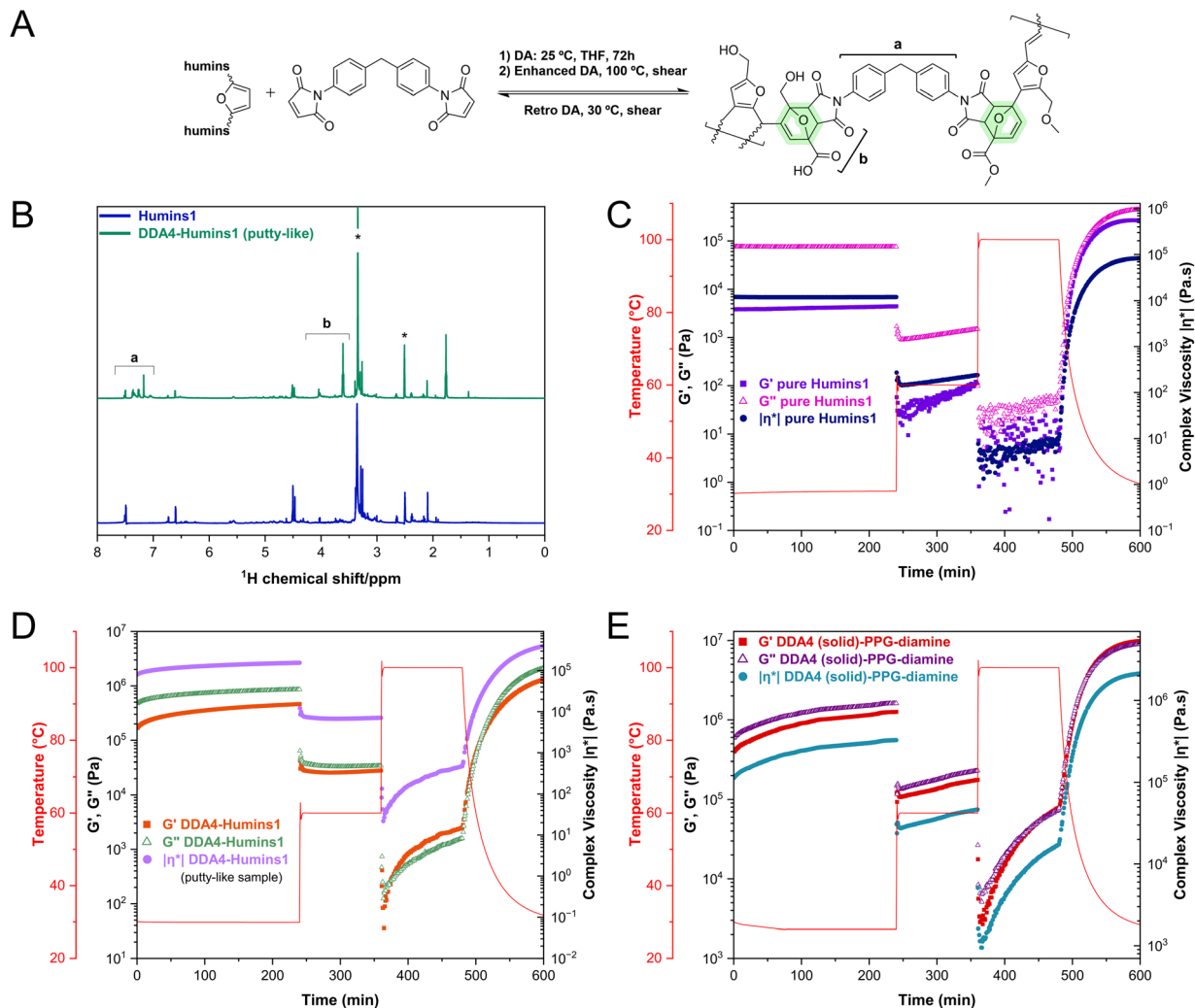
Fig. 3 (A) Diels Alder reaction between humins and BMI forming the crosslinked adducts, (B) ^{1}H NMR spectra of pure Humins1, DDA4-Humins1 (putty-like) in DMSO-d6 at 25 °C, (C–E) temperature-modulated SAOS measurements of (C) pure humins, (D) DDA4-Humins1 (putty-like), (E) DDA4 (solid)-PPG-diamine. All rheological experiments were performed using a 25 mm parallel-plate geometry, with γ = 0.1%, ω = 1 Hz, and a temperature increase of 2 °C min^{-1} in an N$_2$ atmosphere.

protons adjacent to carbonyl groups or unsaturated bonds, consistent with methylene protons neighbouring the imide carbonyl groups in DA adducts formed from bismaleimide and furan.[49] Signals observed in the $\delta(^1H)$ = 2.0–1.5 ppm range are assigned to methylene protons located near alkenes or oxygenated groups, while resonances between $\delta(^1H)$ = 1.3–0.8 ppm arise from terminal methyl groups within alkyl chains associated with bismaleimide-derived moieties or aliphatic segments linked to the furanic structures. Overall, these specific chemical shifts observed in the spectra provide strong evidence for the formation of DA adducts between furan rings and bismaleimide, resulting in new aliphatic bridges and imide bonds. The same chemical shifts and new product peaks were observed in the NMR results of DA adducts obtained with other humins (Fig. S21 and Table S6). At the same time, an incomplete conversion of the reactants is clearly observed. At the same time, incomplete conversion is evident from the

persistence of multiplets in the $\delta(^1H)$ = 7.5–6.8 ppm region, which include contributions from aromatic protons of the bismaleimide phenyl rings as well as residual furanic protons.

After a 72-hour reaction, the material was left to dry under ambient conditions, allowing the THF to evaporate under a fume hood. Initially viscous and sticky, the material transitioned to a non-sticky, putty-like consistency within one week, remained in this intermediate state for another week, and fully hardened into a rigid solid after approximately four weeks. These observations suggest that the reaction between humins and BMI continued during the drying phase. FTIR analysis confirmed ongoing chemical changes, with notable variations in the transmittance of characteristic BMI peaks at 1147 cm^{-1} (C–N) and 686–826 cm^{-1} (out-of-plane C–H) over time (Fig. S22, and photographs taken at different moments of the DDA4-Humins1 presented in Fig. S23).

After completing the chemical characterisation, we investigated the rheological behaviour of the prepared materials and determined their viscoelastic properties. At first instance, standard SAOS tests were conducted to compare the viscoelastic responses of pure humins with those of the DA-derived products. Additionally, a comparison of putty-like and solid materials at different temperatures was performed (Fig. S24–S31). Notably, despite differences in the viscosities of the parent humins, the resulting products are much more comparable to one another (Fig. 2C): η_0(DDA4-Humins1) = 3.5 × 10^4 Pa s; η_0(DDA5-Humins2) = 4.2 × 10^4 Pa s; η_0(DDA6-Humins3) = 8.2 × 10^4 Pa s; η_0(DDA7-Humins4) = 3.84 × 10^4 Pa s. The results of the amplitude sweep tests show that all DA adducts exhibit significantly higher G' and G'' moduli compared to their corresponding humins precursors, confirming the formation of a partially crosslinked network (Table S7). The average storage modulus increased by one to three orders of magnitude. The linear viscoelastic region extended to γ = 0.5–1.0% for the DA systems. At larger strains, the complex viscosity followed a decay of $|\eta^*| \propto \gamma^m$ with $m = -0.7$ to -1.0 for the DA samples, indicating shear thinning.

From the viscoelastic analysis, it appears that the lower the molecular weight of the humins phase, the greater the potential for reaction, ultimately leading to products that converge macroscopically in terms of viscosity (e.g. in case of Humins 3,4). It should be noted, however, that the 75 wt% loading was optimized based on Humins1. Given the differences in apparent total furanic content, this ratio may need to be adjusted; consequently, trend-wise comparisons cannot yet be made, and no clear correlation has been observed.

To further probe the presence of a dynamic covalent bonding structure obtained via the DA reaction, we first examined the temperature-dependent rheological behaviour of pure Humins1 and its corresponding DA adduct (DDA4-Humins1 (putty-like)) under a stepwise temperature ramp 30–60–100 °C (Fig. 3C and D). For pure Humins1, both the modulus and the complex viscosity decreased continuously with increasing temperature, indicating progressive relaxation of the weakly associated humins network. No crossover between G' and G'' was observed, with G'' remaining higher than G' at all temperatures, consistent with the absence of thermally activated dynamic bonding. In contrast, the DDA4-Humins1 sample (2 weeks, putty-like) exhibited a more complex thermal response. A slight decrease in both moduli and complex viscosity occurred up to 60 °C, followed by a further drop near 100 °C. At this stage, however, a G' to G'' crossover emerged, reflecting the transition from viscous to an elastic response as DA linkages reformed upon heating. During the subsequent cooling phase, a reverse crossover ($G'' > G'$) was observed. To further verify the reversibility of these interactions, cyclic temperature tests were performed. For putty-like DA adducts (2 weeks), the temperature was cycled between 25 °C and 100 °C, and for solid ones (4 weeks) between 60 °C and 100 °C (Fig. 4A and B). In each cycle, $G'' > G'$ at low temperatures and $G' > G''$ at high temperatures, with nearly complete recovery of all moduli and $|\eta^*|$ after cooling. This reproducible crossover behaviour confirms the thermoreversible nature of the DA linkages. Comparable behaviour was found for the other humins-DA adducts (Fig. S32–S36).

From an application perspective, continued material hardening is unfavourable. We suggest that the residual BMI contributes to this effect, and that its selective deactivation could, in principle, help preserve the material's properties over time. To address this, we probed a strategy to capture residual maleimide functionalities via an aza-Michael addition reaction, a well-established approach in macromolecular design.[50] This was achieved via a post-treatment step in which the solid DA product was further reacted with poly(propylene glycol) bis(2-aminopropyl ether) diamine (PPG-diamine). To our satisfaction, incorporation of the diamine regenerated the solid DDA product into a putty-like state. Furthermore, temperature-modulated SAOS measurements confirmed a deceleration in the cross-linking kinetics (Fig. 3E). For comparison, the untreated solid DA material exhibits a gradual increase in
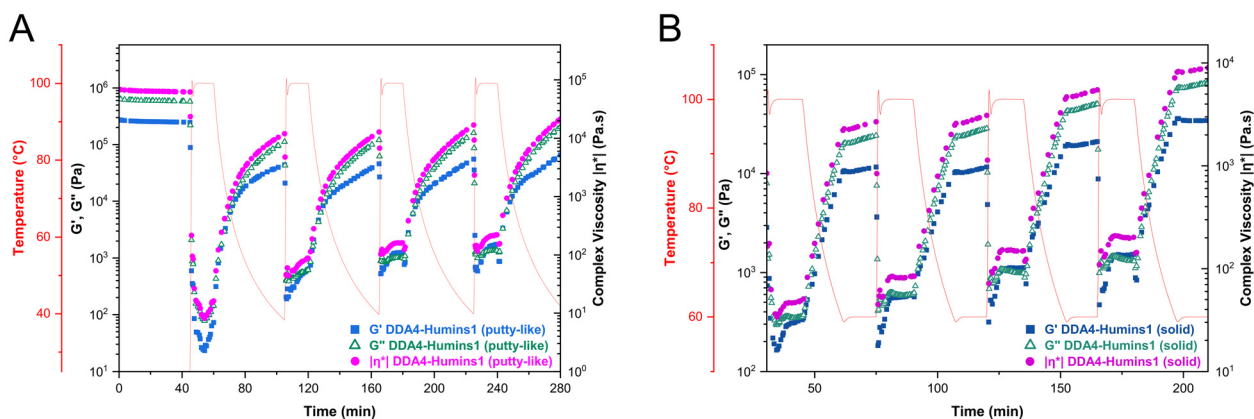

Fig. 4 Time sweep tests of DDA4-Humins1 were conducted under dynamic temperature cycles. (A) Putty-like viscoelastic material (2 weeks) measured between 40 and 100 °C. (B) Solid material (4 weeks) measured between 60 and 100 °C. All measurements were performed using a 25 mm parallel-plate geometry, with γ = 1%, ω = 10 Hz, and a heating rate of 2 °C min in an N$_2$ atmosphere.

modulus over successive temperature cycles, reflecting the continued evolution of the network (Fig. 4B).

The effect of the bismaleimide structure on thermally reversible network formation and self-healing was investigated in more detail by repeating the experiment using BMI1500, an imide-extended bismaleimide having a long spacer between the maleimide groups, instead of standard bismaleimide (representative structures for DA adducts, Fig. S37). Similarly, ^{1}H NMR confirmed the formation of the DA adduct (Fig. S38 and Table S8). However, temperature ramp rheology revealed that, in contrast to Humins-BMI adducts, the Humins-BMI1500 adducts did not exhibit a G'/G'' transition at 100 °C (Fig. S39). Instead, a pronounced decrease in the moduli was observed, accompanied by an increase in signal noise. This behaviour is consistent with the presence of imide chain extension, which favours viscous flow over network formation by effectively reducing the cross-link density. This highlights the critical role of maleimide spacing in enabling stress-assisted DA network formation.

To examine the thermal stability of the DA adducts, TGA measurements were carried out and compared with those of the corresponding humins precursors (Fig. S40 and S41). The degradation onset temperatures ($T_{d5\%}$) showed only limited variation across the series. This is not unexpected, as pristine humins are known to contain residual moisture and low-molecular-weight fractions that can contribute to early mass loss during heating.[30] More significant differences appeared at higher mass-loss levels. In all DA-modified samples, the temperature at 50% weight loss (T_{50}) shifted to a narrow range of 470–475 °C, regardless of the starting humins batch. Despite compositional variability in the starting humins, the DA modification led to products with remarkably similar high-temperature behaviour. The change was particularly pronounced for Humins4, where T_{50} increased from 227 °C to 474 °C after Diels–Alder crosslinking. A similar trend was observed for the residual char at 550 °C: while the pristine humins showed variable, and in some cases low, char yields (notably 7.7% for Humins4), all DA adducts consistently retained around 43% (Table S9). Overall, the thermal data indicate that DA modification significantly changes the high-temperature behavior of the materials and reduces the thermal differences between the various humins batches, leading to a more uniform thermal response. To ensure that the rheological measurements at 100 °C did not induce degradation, isothermal TGA experiments were performed at the same temperature (Fig. S42). In both the fully dried solid sample and the 3-day dried (putty-like) sample, the main mass loss occurred within the first minutes and then levelled off. No continuous mass decrease was observed during isothermal hold, indicating that prolonged exposure at 100 °C does not lead to progressive thermal degradation under applied conditions.

Diels–Alder-induced control over dielectric and healing properties

Based on the chemical structure of humins, the presence of polar groups and conjugated double bonds is expected to enable electrical conductivity. At the same time, the DA reaction offers a means to disrupt this conductivity by targeting a key structural element in the conjugated system – the furan ring. To validate this, we performed electrical conductivity tests using a rheo-dielectric setup across a frequency range of 0.01 Hz to 10 MHz (Fig. 5 and Fig. S43, S44) on all representative types of materials under consideration: pure humins, putty-like DA adducts (after two weeks of the DA reaction), and solid DA adducts (after four weeks of the DA reaction). Conductivity was probed at three thermal-history states: room temperature before thermal cycling (RT_0), after melting at 60 °C (AM), and after cooling back to 25 °C (AC). Unless noted, RT_0, AM, and AC measurements were performed sequentially on the same specimen.

It was encouraging to observe that the electrical conductivity of pure humins was relatively high, as shown in Fig. 5. Among all the samples, Humins4 exhibited the highest conductivity, reaching 10^{-5} S cm^{-1} – three to four orders of magnitude higher than that of conventional insulating polymers like polylactic acid (PLA)[51] or polyamides (PA6, PA46),[52,53] which typically range from 10^{-10} to 10^{-15} S cm^{-1}. Notably, Humins4 also possessed the lowest viscosity among all the other samples, enabling greater molecular mobility, which is consistent with the observed conductivity values. In contrast, the solid DA adducts showed the lowest conductivity, dropping to as low as 10^{-10} S cm^{-1}, comparable to traditional polymeric insulators. The relatively high conductivity of pure humins can be attributed to the presence of several conjugated double bonds, which allow π-electrons to delocalize and move freely along the carbon framework. During the DA reaction, however, a reduction in the number of accessible conjugated pathways is expected in the DA adducts. As a result, electron delocalisation became highly restricted, leading to a marked decrease in conductivity. Temperature was also found to play a significant role in the electrical conductivity of all samples. The electrical conductivity at 60 °C (where the samples melted) was found to be higher than that at room temperature (25 °C) for all the samples. This observation aligns with the fact that at slightly higher temperatures, more charge carriers become thermally excited and hop between the sites, thereby increasing conductivity.[39] Overall, the moderate electrical conductivity of humins makes them suitable for applications where low conductivity is desired, such as in antistatic/electrostatic discharge (ESD) packaging or dissipative coating applications. Furthermore, their intrinsic properties make humins promising candidates as matrix materials for the development of conductive nanocomposites for applications that require AC conductivity or high-frequency dielectric losses, such as electromagnetic shielding.

Thermally induced healing is a common characteristic of materials containing DA functionality. To evaluate the self-healing capability of the synthesised materials, disintegrated solid samples were subjected to thermal treatment in an oven. The fractured surfaces were gently brought into contact to ensure interfacial alignment prior to heating. The specimens were conditioned at 60 °C for 1 hour under stress-free con-
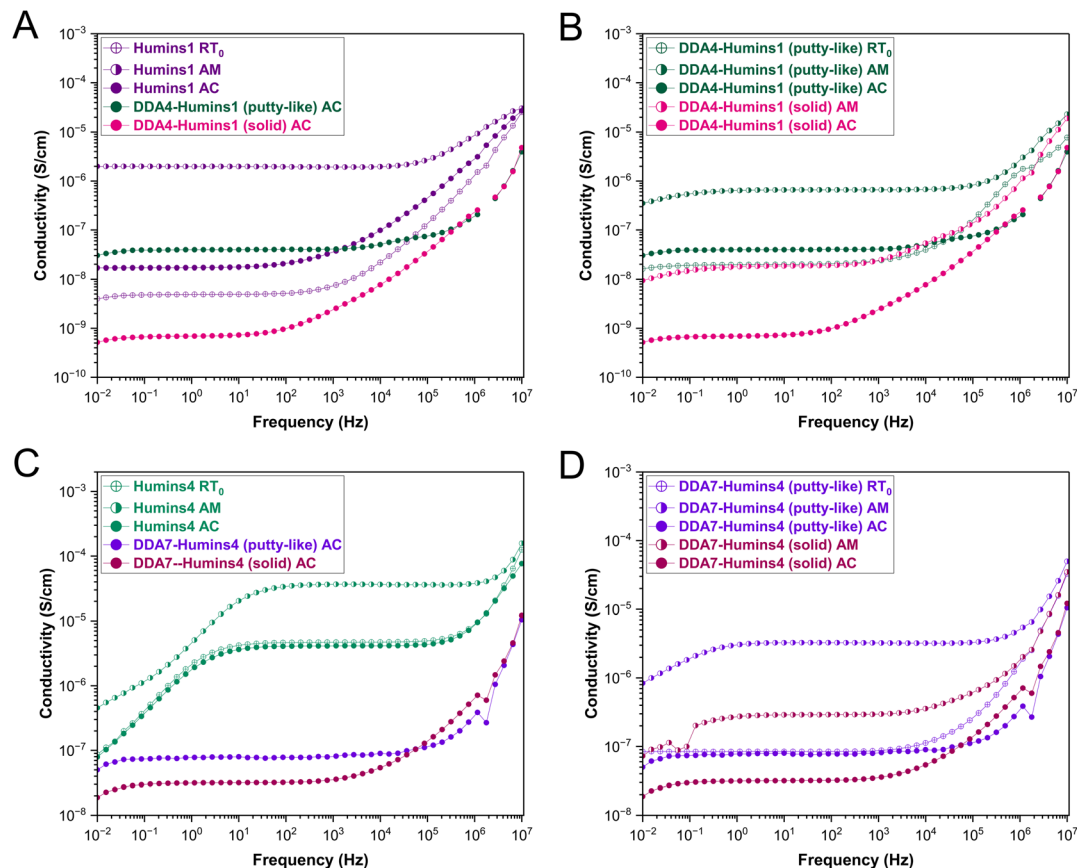
Fig. 5 Frequency-dependent electrical conductivity of pure humins and Diels−Alder adducts measured using a rheo-dielectric setup, (A−D) conductivity spectra of Humins1, Humins4, DDA4- and DDA7- based systems, respectively, at three thermal history states: room temperature before thermal cycling (RT$_0$), after melting at 60 °C (AM), and after cooling back to 25 °C (AC). Measurements were performed under a N$_2$ atmosphere, with a frequency range of 10^{-2} to 10^{7} Hz, and a 25 mm parallel-plate geometry.

ditions, without external mechanical force (Fig. S45 and S46). Unlike the rheological experiments, which probe network rearrangement under combined thermo-shear influence, this experiment was intentionally performed under purely thermal conditions to assess principal stress-free network reorganisation and thermal reprocessability. As indicated by temperature-modulated SAOS measurements (Fig. 3D), the material exhibits potential for more profound conversion of available diene and dienophile groups, leading to increased elasticity at this temperature. Thus, 60 °C represents a temperature window where enhanced molecular mobility and dynamic bond exchange may facilitate interfacial reconnection. Visual inspection before and after treatment revealed partial structural recovery, with the previously fractured interface appearing more continuous after heating. This observation supports the occurrence of partial thermally induced recovery, arising from the combined effects of viscoelastic flow and reversible DA bond reorganisation. On the other hand, the DA reaction provides a selective and controllable method for suppressing conductivity, rendering the resulting materials suited for dielectric applications.

Conclusion

In this study, we developed an alternative strategy to valorise humins, an abundant yet underutilised byproduct of sugar biorefineries. Owing to their furan-rich functionality amounting to 64 wt% of furans, humins offer untapped potential in classical DA cycloaddition reactions as a sustainable source of dienes. To this end, we successfully demonstrated their propensity to undergo DA reactions using four representative humins batches of different viscosities, reacting them with bismaleimide under mild conditions. In all cases, the formation of covalently bonded networks was observed, with highly *endo*-selective cycloadditions. Using data from the model reaction with FA, representative of structural motifs present in humins, we optimised the reaction by varying the humins content and reaction time. We found that materials of suitable quality were obtained with humins loadings of up to 75 wt%. Furthermore, the system exhibited an inverted thermal response under oscillatory shear, where the forward DA reaction progressed at elevated temperatures, while the retro-DA reaction occurred at lower temperatures. The resulting materials displayed tunable

conductivity, allowing humins modulation from semiconductive (10^{-5} S cm^{-1}) to insulating (10^{-10} S cm^{-1}) behaviour *via* the DA approach. Future efforts will focus on exploring the potential applications that leverage the viscoelastic nature of the material and the reversible characteristics of the DA network, particularly in thermally reprocessable and extrusion-assisted dynamic material systems.

Author contributions

Dilhan Kandemir: conceptualisation; methodology; investigation; data curation; formal analysis; visualisation; writing – original draft; writing – review & editing. Meghana Mekala: investigation (dielectric rheology). Ruth Cardinaels: investigation (dielectric rheology); review & editing. Peter Van Puyvelde: supervision; writing – review & editing. Anton Ginzburg: supervision; conceptualisation; methodology; funding acquisition; project administration; writing – review & editing; corresponding author.

Conflicts of interest

There are no conflicts of interest.

Data availability

The data supporting this article are included in the supplementary information (SI). Supplementary information: extensive experimental details, materials and methods, ^{1}H NMR spectra, rheology data, FTIR data, dielectric data, and TGA data. See DOI: https://doi.org/10.1039/d6gc00070c.

The datasets are also available from https://drive.google.com/drive/folders/12d_t7ONhAuAU_C_AOgw0T1-j8KvSnBUK.

Acknowledgements

References

1 K. C. Nicolaou, S. A. Snyder, T. Montagnon and G. Vassilikogiannakis, *Angew. Chem., Int. Ed.*, 2002, **41**, 1668–1698.

2 T. Wang, R. R. Naredla, S. K. Thompson and T. R. Hoye, *Nature*, 2016, **532**, 484–488.

3 M.-M. Xu, L. Yang, K. Tan, X. Chen, Q.-T. Lu, K. Houk and Q. Cai, *Nat. Catal.*, 2021, **4**, 892–900.

4 B. Gacal, H. Durmaz, M. Tasdelen, G. Hizal, U. Tunca, Y. Yagci and A. Demirel, *Macromolecules*, 2006, **39**, 5330–5336.

5 G. Franc and A. K. Kakkar, *Chem. – Eur. J.*, 2009, **15**, 5630–5639.

6 M. I. Soares, A. L. Cardoso and T. M. V. Pinho e Melo, *Molecules*, 2022, **27**, 1304.

7 L. L. Fluegel and T. R. Hoye, *Chem. Rev.*, 2021, **121**, 2413–2444.

8 V. Laina-Martin, J. Humbrias-Martin, R. Mas-Balleste, J. A. Fernandez-Salas and J. Aleman, *ACS Catal.*, 2021, **11**, 12133–12145.

9 T. Sakai and R. L. Danheiser, *J. Am. Chem. Soc.*, 2010, **132**, 13203–13205.

10 H. Pellissier, *Tetrahedron*, 2009, **65**, 2839–2877.

11 E. Vedejs, J. Stults and R. Wilde, *J. Am. Chem. Soc.*, 1988, **110**, 5452–5460.

12 M. Werr, E. Kaifer and H. J. Himmel, *Chem. – Eur. J.*, 2020, **26**, 12328–12332.

13 Y. Yang, T. K. Ronson, D. Hou, J. Zheng, I. Jahović, K. H. Luo and J. R. Nitschke, *J. Am. Chem. Soc.*, 2023, **145**, 19164–19170.

14 D. Vazquez, R. A. Spanevello, A. M. Sarotti and M. I. Mangione, *Eur. J. Org. Chem.*, 2024, e202400650.

15 T. V. Alves and I. Fernández, *Org. Biomol. Chem.*, 2023, **21**, 7767–7775.

16 C.-J. Huang and E. Y. Li, *RSC Adv.*, 2019, **9**, 7246–7250.

17 S. Yu, H. M. de Bruijn, D. Svatunek, T. A. Hamlin and F. M. Bickelhaupt, *ChemistryOpen*, 2018, **7**, 995–1004.

18 D. J. MacKinnon, B. Drain and C. R. Becer, *Macromolecules*, 2024, **57**, 6024–6034.

19 A. Safaei, S. Terryn, B. Vanderborght, G. Van Assche and J. Brancart, *Polymers*, 2021, **13**, 2522.

20 K. Cerdan, M. Thys, A. C. Cornellà, F. Demir, S. Norvez, R. Vendamme, N. Van den Brande, P. Van Puyvelde and J. Brancart, *Prog. Polym. Sci.*, 2024, **152**, 101816.

21 R. C. Cioc, E. Harsevoort, M. Lutz and P. C. Bruijnincx, *Green Chem.*, 2023, **25**, 9689–9694.

22 R. C. Cioc, M. Crockatt, J. C. van der Waal and P. C. Bruijnincx, *Angew. Chem.*, 2022, **134**, e202114720.

23 L. Moreira Grilo, S. Faoro, R. Folkersma, T. M. Lacerda, L. Mazzocchetti, K. Loos and D. Maniar, *ACS Appl. Polym. Mater.*, 2024, **6**, 13723–13734.

24 Y. Zhao, K. Lu, H. Xu, L. Zhu and S. Wang, *Renewable Sustainable Energy Rev.*, 2021, **139**, 110706.

25 M. Sayed, N. Warlin, C. Hulteberg, I. Munslow, S. Lundmark, O. Pajalic, P. Tunå, B. Zhang, S.-H. Pyo and R. Hatti-Kaul, *Green Chem.*, 2020, **22**, 5402–5413.

26 E. de Jong, M. Mascal, S. Constant, T. Claessen, P. Tosi and A. Mija, *Green Chem.*, 2024, **27**, 3136–3166.

27 J. C. Velasco Calderón, J. S. Arora and S. H. Mushrif, *ACS Omega*, 2022, **7**, 44786–44795.

28 S. Constant, C. S. Lancefield, W. Vogelzang, R. K. P. Purushothaman, A. E. Frissen, K. Houben, P. de Peinder, M. Baldus, B. M. Weckhuysen and D. S. van Es, *Green Chem.*, 2024, **26**, 7739–7751.

29 D. Kandemir, P. Van Puyvelde and A. Ginzburg, *ChemSusChem*, 2024, e202400403.

30 S. Constant, C. S. Lancefield, W. Vogelzang, R. K. P. Purushothaman, A. E. Frissen, K. Houben, P. de Peinder, M. Baldus, B. M. Weckhuysen and D. S. van Es, *Green Chem.*, 2024, **26**, 7739–7751.

31 Y. S. Zholdassov, L. Yuan, S. R. Garcia, R. W. Kwok, A. Boscoboinik, D. J. Valles, M. Marianski, A. Martini, R. W. Carpick and A. B. Braunschweig, *Science*, 2023, **380**, 1053–1058.

32 G. Socrates, *Infrared and Raman characteristic group frequencies: tables and charts*, John Wiley & Sons, 2004.

33 K. Cerdan, J. Brancart, E. Roels, B. Vanderborght and P. Van Puyvelde, *Polymers*, 2022, **14**, 1657.

34 S. Schäfer and G. Kickelbick, *Polymer*, 2015, **69**, 357–368.

35 V. Froidevaux, M. Borne, E. Laborbe, R. Auvergne, A. Gandini and B. Boutevin, *RSC Adv.*, 2015, **5**, 37742–37754.

36 K. I. Galkin, I. V. Sandulenko and A. V. Polezhaev, *Processes*, 2021, **10**, 30.

37 R. C. Boutelle and B. H. Northrop, *J. Org. Chem.*, 2011, **76**, 7994–8002.

38 A. Buonerba, R. Lapenta, S. Ortega Sánchez, C. Capacchione, S. Milione and A. Grassi, *ChemistrySelect*, 2017, **2**, 1605–1612.

39 T. Wang, C. H. van der Loo, Z. Zhang, J. Broekman, Q. Yuan, J. G. Winkelman, A. Heeres, R. W. Havenith, A. J. Minnaard and P. J. Deuss, *ACS Sustainable Chem. Eng.*, 2024, **12**, 11195–11205.

40 A. Arrieta, F. P. Cossío and B. Lecea, *J. Org. Chem.*, 2001, **66**, 6178–6180.

41 E. Skolia and C. G. Kokotos, *Eur. J. Org. Chem.*, 2024, e202400105.

42 B. J. Adzima, H. A. Aguirre, C. J. Kloxin, T. F. Scott and C. N. Bowman, *Macromolecules*, 2008, **41**, 9112–9117.

43 C. Ruiz-Pardo, L. Silva-Gutiérrez, J. Lizardi-Mendoza, Y. López-Franco, C. Peniche-Covas and W. Argüelles-Monal, *Polymers*, 2022, **14**, 1202.

44 M. Diaz, G. Van Assche, F. Maurer and B. Van Mele, *Polymer*, 2017, **120**, 176–188.

45 P. van den Tempel, Doctor of Philosophy PhD Thesis, University of Groningen, 2025.

46 R. K. Bose, J. Kötteritzsch, S. J. Garcia, M. D. Hager, U. S. Schubert and S. Van Der Zwaag, *J. Polym. Sci., Part A: Polym. Chem.*, 2014, **52**, 1669–1675.

47 E. E. Maassen, R. Anastasio, S. Poto, R. Cardinaels, R. P. Sijbesma, L. C. van Breemen and J. P. Heuts, *J. Polym. Sci.*, 2021, **59**, 1200–1208.

48 K. N. Houk, R. J. Loncharich, J. F. Blake and W. L. Jorgensen, *J. Am. Chem. Soc.*, 1989, **111**, 9172–9176.

49 K. A. Ahrendt, C. J. Borths and D. W. MacMillan, *J. Am. Chem. Soc.*, 2000, **122**, 4243–4244.

50 B. D. Mather, K. Viswanathan, K. M. Miller and T. E. Long, *Prog. Polym. Sci.*, 2006, **31**, 487–531.

51 Q. Zhang and S. Zhang, *J. Mater. Sci. Chem. Eng.*, 2022, **10**, 30–43.

52 B. Weidenfeller, H. Rode, L. Weidenfeller and K. Weidenfeller, *J. Appl. Polym. Sci.*, 2020, **137**, 48882.

53 S. Suksanit, P. Pattananuwat and P. Potiyaraj, *Key Eng. Mater.*, 2020, **831**, 117–121.